ATLAS NOTE

ATLAS-CONF-2015-017

12th April 2015

Data-driven determination of the energy scale and resolution of jets reconstructed in the ATLAS calorimeters using dijet and multijet events at $\sqrt{s} = 8$ TeV

The ATLAS Collaboration

Abstract

The response of the ATLAS calorimeter to jets is studied using data-driven techniques for proton-proton collisions at $\sqrt{s} = 8$ TeV recorded by ATLAS in 2012. The jet response is studied as a function of jet transverse momentum and pseudorapidity relative to a central reference region by evaluating the transverse momentum balance in dijet events. A new calibration is derived to correct the jet energy scale in data for residual effects not captured by the initial calibration based on simulation. The calibration factors are found to range from 0.96 to 1.02 depending on the pseudorapidity of the jet. The uncertainties on these calibration factors have been significantly reduced compared to previous results; they are typically below 1 % for central jets rising to 3.5 % for low transverse momentum jets at high absolute pseudorapidity. The jet energy scale calibration for central jets with high transverse momentum is then determined using events in which an isolated high transverse momentum jet recoils against a system of low transverse momentum jets. The data and simulation are found to agree to better than 1 % for jets with transverse momentum up to 1.7 TeV, with an associated uncertainty of less than 1 %. Finally, the jet energy resolution is determined using dijet events as a function of jet transverse momentum and pseudorapidity. In general, it is found that the jet energy resolution in data is well reproduced in the simulation.

1. Introduction

The response of the ATLAS calorimeters to a jet depends on the jet energy and direction. The initial jet energy scale calibration is achieved using Monte Carlo (MC) simulations [1]. Additional corrections are then derived using data-driven techniques that exploit the transverse momentum balance in Z/γ-jet, dijet and multijet events. The Z/γ-jet events are used to derive corrections and associated uncertainties in the central detector region. The dijet events are used to derive calibrations for forward jets relative to the central jets. Finally, multijet events are used after applying all other calibrations to extend the calibration to the highest possible transverse momentum.

In this note, the results of the jet energy scale calibrations using dijet and multijet events are presented for proton–proton collisions at a centre-of-mass energy $\sqrt{s} = 8$ TeV recorded by the ATLAS detector in 2012. First, the relative calorimeter jet response is measured as a function of detector pseudorapidity[1], η_{det}, by balancing the transverse momentum, p_{T}, of the two leading jets in dijet topologies. A new pseudorapidity-dependent calibration factor is subsequently derived, along with an associated systematic uncertainty. Following this, the response of the central calorimeter to high transverse momentum jets is measured by balancing the transverse momentum of a high p_{T} jet recoiling against several low p_{T} jets. A new high-p_{T} jet calibration and its associated uncertainty is derived. Finally, the jet energy resolution is studied using the transverse momentum balance of jets in dijet events.

2. The ATLAS detector

The ATLAS detector consists of an inner tracking detector, sampling electromagnetic and hadronic calorimeters and muon chambers in a toroidal magnetic field. A detailed description of the ATLAS experiment can be found elsewhere [2].

The inner detector (ID) has complete azimuthal coverage and spans the region $|\eta_{\mathrm{det}}| < 2.5$. It consists of layers of high-granularity silicon pixel detectors, silicon microstrip detectors and transition radiation tracking detectors. These tracking detectors are located inside a solenoid magnet that provides a uniform magnetic field of 2 T. The ID is used to reconstruct tracks from charged particles and determine their transverse momenta from the curvature of the tracks.

Jets are reconstructed from energy deposited in the calorimeter system. Electromagnetic calorimetry is provided by high granularity liquid argon (LAr) sampling calorimeters, using lead as an absorber, which are split into barrel ($|\eta_{\mathrm{det}}| < 1.475$) and end-cap ($1.375 \leq |\eta_{\mathrm{det}}| < 3.2$) regions. The hadronic calorimeter is divided into the barrel ($|\eta_{\mathrm{det}}| < 0.8$), extended barrel ($0.8 \leq |\eta_{\mathrm{det}}| < 1.7$), and end-cap ($1.5 \leq |\eta_{\mathrm{det}}| < 3.2$) regions. The barrel and extended barrel are instrumented with with tile scintillator/steel calorimeters, whereas the hadronic end-cap uses LAr/copper calorimeter modules. A forward calorimeter instrumented with LAr/copper and LAr/tungsten modules provides electromagnetic and hadronic calorimetry in the region $3.1 \leq |\eta_{\mathrm{det}}| < 4.9$.

Dijet and multijet events are retained for analysis using the ATLAS trigger system, which consists of a hardware-based 'level 1 trigger' (`L1`) followed by a software-based 'high-level trigger' (`HLT`) [3]. Jets

---

[1] The ATLAS coordinate system is right-handed, with the x-axis pointing to the centre of the LHC ring, the z-axis following the beam direction and the y-axis pointing upwards. The azimuthal angle $\phi = 0$ corresponds to the positive x-axis and ϕ increases clockwise looking into the positive z direction. The detector pseudorapidity, η_{det}, is related to the polar angle with respect to the beam, θ, by $\eta_{\mathrm{det}} = -\ln \tan \frac{\theta}{2}$.

are identified at `L1` using a sliding window algorithm with coarse granularity calorimeter towers as input. In the `HLT`, jets are reconstructed from calorimeter cells using the same algorithms as used in the final analysis. For events with leading jet transverse momentum greater than 65 GeV, the events are selected using the `L1` and `HLT` jet algorithms. For events with leading jet transverse momentum less than 65 GeV, events are selected at `L1` using a random trigger.

3. Dataset

The dataset consists of proton-proton (*pp*) collisions at a centre-of-mass energy of $\sqrt{s} = 8$ TeV, recorded from April to December 2012. All ATLAS subdetectors were required to be operational and events were rejected if any data quality issues were present. The total integrated luminosity is approximately 20 fb^{-1}. The LHC beams were operated with proton bunches organised in ‘bunch trains’, with bunch crossing intervals (or bunch spacing) of 50 ns. The average number of interactions per bunch crossing ($\langle\mu\rangle$) was typically $10 \leq \langle\mu\rangle \leq 30$ for the 2012 data taking.

4. Monte Carlo simulation

Inclusive dijet production is simulated using the Powheg Box [4, 5, 6], Sherpa 1.4.5 [7], Pythia 8.160 [8] and Herwig++ 2.5.2 [9, 10] event generators.

The Powheg Box event generator produces inclusive dijet events at next-to-leading-order (NLO) accuracy in perturbative QCD [11], using the CT10 parton distribution functions (PDFs) [12]. The fully hadronic final state is produced by interfacing the Powheg Box to Pythia 8.175, which provides parton showering, hadronisation and multiple parton interactions (MPI). These predictions are produced using the AU2 tune [13] for underlying event activity and are referred to as PowhegPythia8 in the remainder of this paper. An additional sample of POWHEG events is generated using Herwig 6.520.2 for parton showering and hadronisation, and Jimmy for MPI modelling (tune AUET2 [14]). These predictions are referred to as Powheg-Herwig in the remainder of this paper.

Sherpa is a matrix-element plus parton-shower generator that is used to produce *n*-jet predictions ($n = 2, 3, 4...$) at leading-order (LO) accuracy in perturbative QCD. The CKKW method [15] is used to combine these various final-state topologies to produce an inclusive dijet sample. Parton-shower, hadronisation and MPI algorithms create the fully hadronic final state. The Sherpa predictions are produced using the CT10 PDFs and the authors’ default generator tune for underlying event activity.

Two samples of dijet events are produced using standalone Pythia8 and Herwig++. These use leading order 2→2 matrix elements to simulate the hard scatter and then use parton showering, hadronisation and MPI algorithms to provide the fully hadronic final state. The Pythia8 sample is produced using the AU2 tune for underlying event activity [16], whereas the Herwig++ sample is produced using the LHC-UE-EE-3 tune [17]. These samples are not as formally accurate as the Sherpa or PowhegPythia8 samples for distributions sensitive to hard quark and gluon radiation, as the additional jets are produced purely by the parton shower.

The particle-level events produced by the event generators are propagated through a Geant4 [18] simulation of the ATLAS detector [19], which models the interactions of the particles with the detector material. Hadronic showers are simulated with the QGSP BERT physics list [20, 21]. The detector signals from the dijet events are overlaid with simulated detector signals from pile-up events (additional inelastic proton-proton interactions produced in LHC beam crossings) to reflect the experimental conditions of the 2012 data taking period. The pile-up events are simulated using Pythia8 using the A2 tune [22] and the MSTW 2008 LO PDF set [23]. The effects of both in-time pileup (pp interactions occurring in the same bunch crossing as the dijet event), and out-of-time pileup (pp interactions occurring in neighbouring bunch crossings) are included in the simulation. The number of pileup events in each bunch crossing is randomly sampled from a Poisson distribution with mean given by $\langle\mu\rangle$, which is directly proportional to the instantaneous luminosity. The $\langle\mu\rangle$ profile in the simulation matches that observed in the data.

Electroweak corrections are not accounted for in the analyses presented in this note; these corrections will be studied in future measurements, though the impact is expected to be small.

5. Jet reconstruction and calibration

Jets are reconstructed using the anti-k_t algorithm [24] with radius parameters $R = 0.4$ or $R = 0.6$. The FastJet implementation [25, 26] of the anti-k_t algorithm is used.

Particle-level jets are defined for simulated events using particles in the event generator record that have a lifetime τ defined by $c\tau > 10$ mm, excluding muons and neutrinos. The exclusion of muons and neutrinos ensures that the particle-level jets are built from particles that leave significant energy deposits in the calorimeters.

Calorimeter jets are reconstructed using three-dimensional clusters of adjacent calorimeter cells that contain a significant energy signal above noise (referred to as topo-clusters) [1, 27, 28]. The basic topo-cluster definition provides a signal reconstructed on the electromagnetic scale (EM-scale) [29, 30, 31, 32]. In addition, topo-clusters can be calibrated using the local cell signal weighting (LCW) method [33] such that the calibrated response of hadrons is, on average, unity. The LCW method is designed to reduce fluctuations in energy due to the non-compensating nature of the ATLAS calorimeter, improving the energy resolution of the reconstructed jets in comparison to jets reconstructed using EM scale clusters [1].

The jets reconstructed from the EM-scale or LCW-scale topo-clusters are calibrated using the four-step procedure outlined below. First, energy deposits originating from pile-up interactions are subtracted from the jet using the procedure outlined in Ref. [34]. Second, the direction of the jet is adjusted such that it points back to the primary interaction vertex instead of the detector center [1]. The primary interaction vertex is defined as the one with the highest $\sum(p_{\mathrm{T}}^{\mathrm{track}})^2$, where the scalar sum is taken over all tracks associated to the vertex. Third, energy- and pseudorapidity-dependent calibration factors are applied to correct the jet energy to the particle level [1]; these calibration factors are determined using simulated events by matching calorimeter jets to particle-level jets and taking the ratio of the calorimeter and particle-level jet energies. Finally, a Global Sequential energy scale calibration (GSC) is applied, which is parameterized in terms of p_{T}, η_{det}, and global jet observables such as the longitudinal structure of the energy depositions within the calorimeter, tracking information associated to the jet, and information related to the activity in the muon chamber behind a jet [35]. After the full calibration, the scale of the calorimeter jets built from EM- or LCW-scale topo-clusters are referred to as EM+JES or LCW+JES, respectively.

The jet calibration procedure outlined above is dependent on the MC simulation to correct the response of the calorimeters. Additional data-driven calibration factors are used to ensure that the impact of mismodelling in the simulation is minimised. The following sections present the results of two of those methods for anti-k_t R=0.4 jets calibrated using the EM+JES scheme. Results for anti-k_t R=0.4 jets calibrated using the LCW+JES scheme are presented in Appendix A.

6. Review of methods to determine relative jet energy scale and jet energy resolution

6.1. Dijet balance

The jet energy resolution and the relative response of the calorimeter as a function of pseudorapidity can be studied using dijet topologies. At leading-order in QCD, the two jets are expected to have equal transverse momentum, and any imbalance in the transverse momentum would therefore arise from different responses to jets in different calorimeter regions. The transverse momentum balance is quantified by the asymmetry

$$\mathcal{A} = \frac{p_{\mathrm{T}}^{\mathrm{probe}} - p_{\mathrm{T}}^{\mathrm{ref}}}{p_{\mathrm{T}}^{\mathrm{avg}}}, \tag{1}$$

where $p_{\mathrm{T}}^{\mathrm{ref}}$ is the transverse momentum of a jet in a well-calibrated reference region, $p_{\mathrm{T}}^{\mathrm{probe}}$ is the transverse momentum of the jet in the calorimeter region under investigation, and $p_{\mathrm{T}}^{\mathrm{avg}} = (p_{\mathrm{T}}^{\mathrm{probe}} + p_{\mathrm{T}}^{\mathrm{ref}})/2$.

The calorimeter response relative to the reference region, $1/c$, is then defined as

$$\frac{1}{c} = \frac{p_{\mathrm{T}}^{\mathrm{probe}}}{p_{\mathrm{T}}^{\mathrm{ref}}} = \frac{2 + \langle\mathcal{A}\rangle}{2 - \langle\mathcal{A}\rangle}, \tag{2}$$

where c is the correction factor and $\langle\mathcal{A}\rangle$ is the mean of the asymmetry distribution in a given bin of $p_{\mathrm{T}}^{\mathrm{avg}}$ and η_{det}. Two versions of the analysis are performed. In the *central reference method*, a single reference region ($|\eta_{\mathrm{det}}| < 0.8$) is chosen and the calorimeter response is measured as a function of $p_{\mathrm{T}}^{\mathrm{avg}}$ and η_{det} relative to this region. In the *matrix method*, multiple reference regions are chosen and the calorimeter response of a given region is measured relative to all the reference regions. The calorimeter response relative to the central region as a function of $p_{\mathrm{T}}^{\mathrm{avg}}$ and η_{det} is then obtained by solving a set of linear equations. The advantage of the matrix method is that the full dataset is used, thus reducing the statistical uncertainty on the final result. Statistical uncertainties on the matrix method result are estimated using pseudoexperiments. In this note, the main results are obtained using the matrix method and the central reference method is only used for validation.

The asymmetry distribution can be used to also probe the jet energy resolution. The width of the asymmetry distribution, $\sigma(\mathcal{A})$, is given by

$$\sigma(\mathcal{A}) = \frac{\sqrt{\sigma(p_{\mathrm{T}}^{\mathrm{ref}})^2 + \sigma(p_{\mathrm{T}}^{\mathrm{probe}})^2}}{p_{\mathrm{T}}^{\mathrm{avg}}}, \tag{3}$$

where $\sigma(p_{\mathrm{T}}^{\mathrm{ref}})$ and $\sigma(p_{\mathrm{T}}^{\mathrm{probe}})$ are the jet energy resolutions associated with the reference and probe jets, respectively. The width of the asymmetry distribution is obtained from a Gaussian fit to the core of the distribution. The jet energy resolution defines the same reference region as for the central reference method, and is measured as a function of $p_{\mathrm{T}}^{\mathrm{avg}}$ and $|\eta_{\mathrm{det}}|$. The jet energy resolution in the reference region is calculated directly from the fitted asymmetry distribution, using events with the probe and reference jets both located in the reference region. The jet energy resolution in other regions can subsequently be calculated. When calculating the asymmetry, the jets are fully calibrated including all data-driven correction factors (including the calibration factors obtained from analysis of Z/γ-jet events [36]).

The transverse momentum balance strictly holds only for 2 → 2 partonic events. In reality, the transverse momentum balance between two jets is affected on an event-by-event basis by additional quark/gluon radiation outside of the jets, as well as hadronisation and MPI effects that cause particle losses and additions to the jets, respectively. A particle-level asymmetry is obtained for each of the event generators using particle-level jets, and the width of the measured asymmetry is corrected by subtracting, in quadrature, the weighted average of the widths of the particle-level quantities.

6.2. Dijet bisector method

The bisector method attempts to separate out the part of the transverse momentum imbalance that is due to physics effects (mainly from soft quark and gluon radiation). The transverse momentum (imbalance) vector of the dijet system, $\vec{p_{\mathrm{T}}}$, is defined as the vector sum of the two leading jets in the event, $\vec{p_{\mathrm{T}}} = \vec{p}_{\mathrm{T,jet1}} + \vec{p}_{\mathrm{T,jet2}}$. This vector is projected onto an orthogonal coordinate system in the transverse plane, (η, Ψ), where η is chosen in the direction that bisects $\Delta\phi_{1,2} = \phi_1$ - ϕ_2, the angle formed by $\vec{p}_{\mathrm{T,jet1}}$ and $\vec{p}_{\mathrm{T,jet2}}$, as illustrated in Figure 1. Detector and physics effects on the transverse momentum balance are present in the Ψ component, whereas only physics effects should be present in the η component. As a result, a jet energy resolution can be estimated by

$$\frac{\sigma(p_{\mathrm{T}})}{p_{\mathrm{T}}} = \frac{\sqrt{\sigma(\Psi)^2 - \sigma(\eta)^2}}{\sqrt{2}P_T\sqrt{\langle|\cos\Delta\phi_{12}|\rangle}}, \tag{4}$$

where $\Delta\phi_{12}$ is the azimuthal angle between the two jets. The width of the η and Ψ distributions are obtained using Gaussian fits.

Although the impact of soft quark or gluon emission is minimised in the bisector method, the approach relies on the assumption that the effects are the same in the Ψ and η components. A correction to the measured JER is made by subtracting the particle-level quantity in quadrature from the measured quantity.

6.3. Multijet balance

The multi-jet balance (MJB) technique exploits the transverse momentum balance for events in which the highest-p_{T} jet (leading jet) is produced back-to-back with a recoil system composed of multiple lower-p_{T} jets. The multi-jet balance of leading jet and recoil system, R_{MJB} is defined as:

$$R_{\mathrm{MJB}} = \frac{\mathrm{p}_{\mathrm{T}}^{\mathrm{leading}}}{p_{\mathrm{T}}^{\mathrm{recoil}}}, \tag{5}$$

where $\mathrm{p}_{\mathrm{T}}^{\mathrm{leading}}$ is the transverse momentum of the leading jet and $p_{\mathrm{T}}^{\mathrm{recoil}}$ is the vectorial sum of the transverse momentum of all sub-leading jets. The mean value of the R_{MJB} is measured in both data and MC in bins of $p_{\mathrm{T}}^{\mathrm{recoil}}$. The MJB is not an unbiased estimator of the leading jet response, having a value below

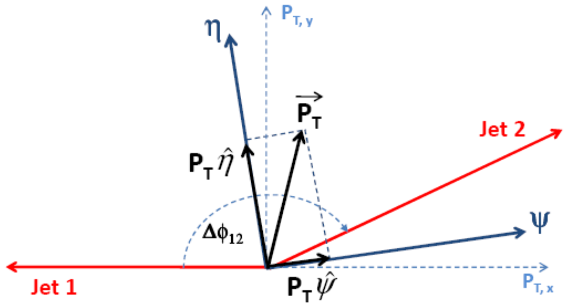

Figure 1: Definition of variables in the bisector technique. The η-axis corresponds to the azimuthal angular bisector of the dijet system, with the Ψ-axis orthogonal to η, in the plane transverse to the beam.

unity even on particle-level due to the effects of soft quark/gluon emission outside of the jets. The largest deviation is at low transverse momentum, with data and MC exhibiting similar dependence. The double ratio $R_{\mathrm{MJB}}^{\mathrm{data}}/R_{\mathrm{MJB}}^{\mathrm{MC}}$ is used to reduce this underlying bias and allow the estimation of the response of high-p_{T} jets. Mis-modelling in the simulation is evaluated as a systematic uncertainty on the double ratio.

The jets used in the construction of $p_{\mathrm{T}}^{\mathrm{recoil}}$ are fully calibrated, including all *in situ* calibrations. However, the *in situ* corrections from the Z/γ-jet analyses are only available for $p_{\mathrm{T}} < 800$ GeV [36]. An iterative procedure is used to calibrate all jets that are used in the calculation of $p_{\mathrm{T}}^{\mathrm{recoil}}$. For the first calculation of the MJB, an upper limit is imposed on the transverse momentum of the recoil jets such that the second highest-p_{T} jet in the event has a $p_{\mathrm{T}} < 800$ GeV. This initial selection allows MJB corrections to be derived, but limits the overall statistical accuracy of the measurements. To improve the statistical accuracy, the MJB is recalculated after removing the upper limit on the transverse momentum of the recoil jets, but using the correction factors from the first iteration to calibrate the recoil jets with $p_{\mathrm{T}} > 800$ GeV.

7. Event selection

Events are required to have at least one reconstructed interaction vertex with at least two associated tracks. Reconstructed jets are required to pass data quality criteria that remove fake jets originating from noise bursts in the calorimeters, from non-collision background, and from cosmic rays [37]. Jets are required to originate from the primary interaction vertex using the jet vertex fraction (JVF) [34]. Tracks are first associated to jets using 'ghost-association' [38]. The JVF variable is then defined as the summed transverse momentum of associated tracks that originate from the primary vertex, divided by the summed transverse momentum of associated tracks from all vertices. Any jet with $|\eta_{\mathrm{det}}| < 2.4$ and $p_{\mathrm{T}} < 50$ GeV is required to have JVF > 0.25 in accordance with the recommendations provided in [34].

Dijet events were retained using a combination of central ($|\eta_{\mathrm{det}}| < 3.1$) and forward ($|\eta_{\mathrm{det}}| > 2.8$) jet triggers. The event selection is designed such that the trigger efficiency, for a specific region of $p_{\mathrm{T}}^{\mathrm{avg}}$, is greater than 99 % and approximately flat as a function of the pseudorapidity of the probe jet. Due to the different prescales for the central and forward jet triggers, the data collected by the different triggers correspond to different integrated luminosities. The data are assigned luminosity- and prescale-dependent weights according to the 'exclusion' method described in [39]. Events are selected in which there are at

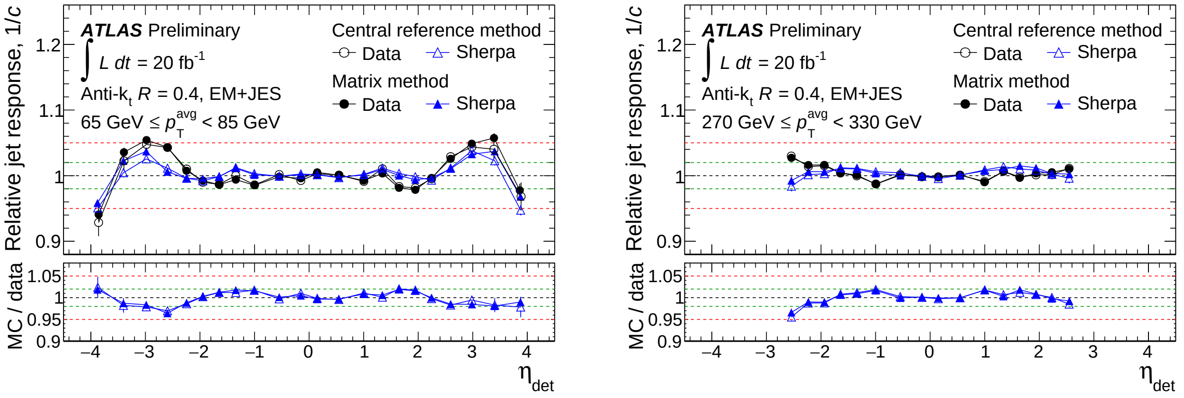

(a)

(b)

Figure 2: Relative response measured using the matrix and the central reference methods for anti-k_t jets with $R = 0.4$ calibrated with the EM+JES scheme as a function of the probe jet pseudorapidity. Results are presented for 65 GeV $\leq p_T^{\text{avg}} <$ 85 GeV and 270 GeV $\leq p_T^{\text{avg}} <$ 330 GeV. The green and red dashed lines indicate 1 ± 2 % and 1 ± 5 % respectively.

least two jets with $p_T >$ 25 GeV and $|\eta_{\text{det}}| < 4.5$. To select events with an exclusive dijet topology, the azimuthal angle between the two leading jets is required to be $\Delta\phi(\text{j1,j2}) > 2.5$ and events are rejected if they contain a third jet with $p_T^{\text{jet3}} > 0.4 p_T^{\text{avg}}$.

Multijet events were retained using single jet triggers that are fully efficient for a given bin of p_T^{recoil}. The triggers used for 300 GeV $< p_T^{\text{recoil}} <$ 600 GeV were prescaled, whereas an unprescaled jet trigger was used for $p_T^{\text{recoil}} >$ 600 GeV. Events are required to contain at least 3 jets with $p_T >$ 25 GeV. The leading jet is required to have $|\eta_{\text{det}}| < 1.2$, and the subleading jets that constitute the recoil system are required to have $|\eta_{\text{det}}| < 2.8$. To select non-dijet events, the leading jet in the recoil system (p_T^{jet2}) is allowed to have no more than 80 % of the total transverse momentum of the recoil system ($p_T^{\text{asymm}} = p_T^{\text{jet2}} / p_T^{\text{recoil}} < 0.8$). Furthermore, the angle in the azimuthal plane between the leading jet and the vector defining the recoil system, α, is required to satisfy $|\alpha - \pi| < 0.3$, and the angle in the azimuthal plane between the leading jet and the nearest jet from the recoil system, β, is required to be greater than 1 radian.

8. Relative jet energy scale calibration using dijet events

8.1. Comparison of matrix and central reference methods

Figure 2 compares the relative jet response calculated using the matrix method to that obtained with the central reference methods for 65 GeV $\leq p_T^{\text{avg}} <$ 85 GeV and 270 GeV $\leq p_T^{\text{avg}} <$ 330 GeV. There is a slight shift in the relative response obtained from the matrix method compared to the central reference method, most notably in the forward regions. However, the same shift appears in both data and MC simulation, resulting in consistent data-to-MC ratios. For 25 GeV $\leq p_T^{\text{avg}} <$ 40 GeV the statistical precision of the matrix method generally exhibits a 40 % improvement compared to the precision of the central reference method. The level of improvement decreases with increasing p_T^{avg} and is typically less than 10 % for $p_T^{\text{avg}} >$ 400 GeV. Hereafter all results correspond to the matrix method.

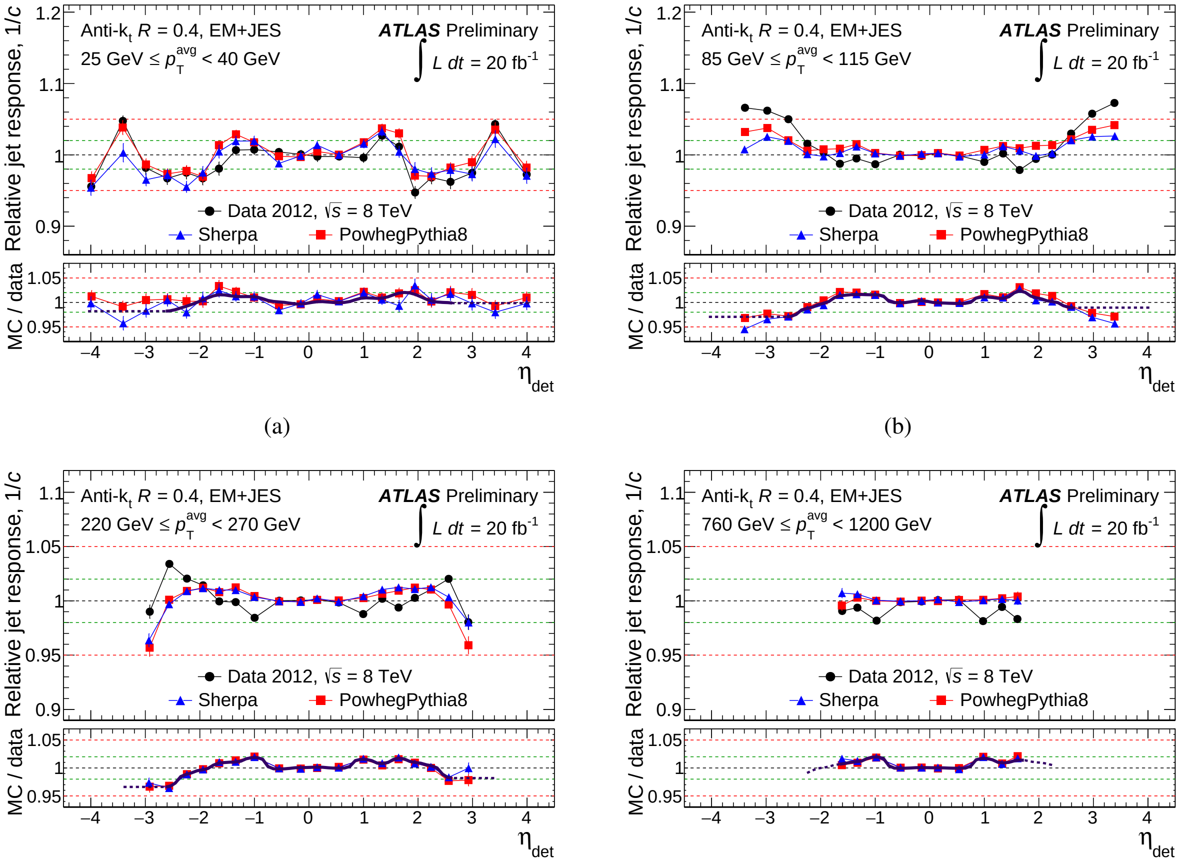

(a)

(b)

(c)

(d)

Figure 3: Relative jet response, $1/c$, as a function of the jet pseudorapidity for anti-k_t jets with $R = 0.4$ calibrated with the EM+JES scheme, separately for 25 GeV $< p_T^{avg} <$ 40 GeV, 85 GeV $< p_T^{avg} <$ 115 GeV, 220 GeV $< p_T^{avg} <$ 270 GeV and 760 GeV $< p_T^{avg} <$ 1200 GeV. The lower parts of the figures show the ratios between the data and MC relative response. These measurements are performed using the matrix method. The green and red dashed lines indicate 1 ± 2 % and 1 ± 5 % respectively.

8.2. Comparison of data with simulation

Figure 3 shows the relative response as a function of the jet pseudorapidity for data and the MC simulations for four different p_T^{avg} regions: 25 GeV $\leq p_T^{avg} <$ 40 GeV, 85 GeV $\leq p_T^{avg} <$ 115 GeV, 220 GeV $\leq p_T^{avg} <$ 270 GeV and 760 GeV $\leq p_T^{avg} <$ 1200 GeV. Figure 4 shows the relative response as a function of p_T^{avg} for two representative η_{det}-bins, namely $-1.5 \leq \eta_{det} < -1.2$ and $2.1 \leq \eta_{det} < 2.4$. The general features of the response in data are reproduced reasonably well by the Sherpa and Powheg-Pythia8 predictions. Furthermore, the theoretical predictions are in good agreement with each other, with a much smaller spread than that observed in the previous studies using Pythia8 and Herwig++ [40]. This is because the new theoretical predictions are accurate to leading order in perturbative QCD for variables sensitive to the third jet activity, such as the dijet balance, whereas the Pythia8 and Herwig++ predictions rely on the leading logarithmic accuracy of the parton shower algorithms.

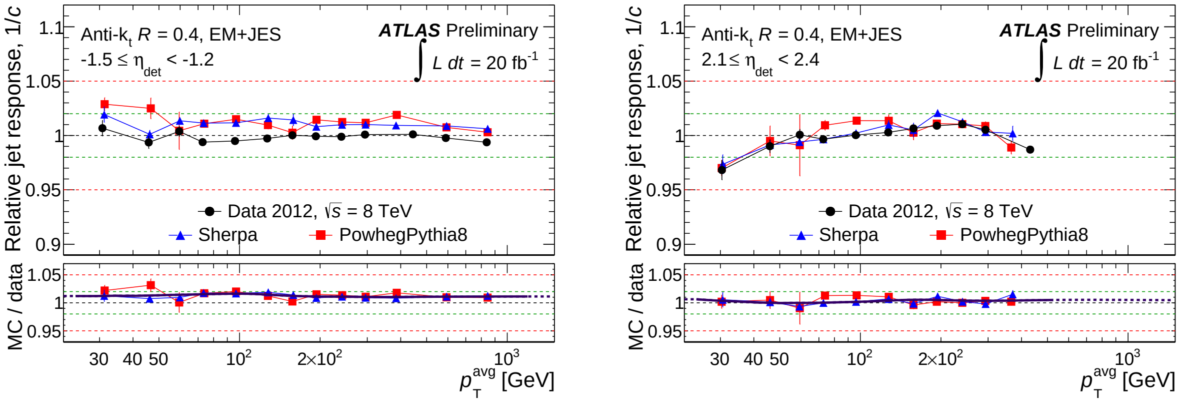

(a) (b)

Figure 4: Relative jet response, $1/c$, as a function of the jet p_{T} for anti-k_t jets with $R = 0.4$ calibrated with the EM+JES scheme, separately for $-1.5 \leq \eta_{\mathrm{det}} < -1.2$ and $2.1 \leq \eta_{\mathrm{det}} < 2.4$. The lower parts of the figures show the ratios between the data and MC relative response. The green and red dashed lines indicate $1 \pm 2\,\%$ and $1 \pm 5\,\%$ respectively.

8.3. Derivation of residual jet energy scale correction

The residual calibration factor is derived from the ratio of data and Sherpa η-intercalibration factors, i.e. $C_i = c_i^{\mathrm{data}}/c_i^{\mathrm{SHERPA}}$. The calibration factors from many bins of $p_{\mathrm{T}}^{\mathrm{avg}}$ and η_{det} are combined into a smooth function using a two dimensional Gaussian kernel.[2] The kernel-width parameters are found to capture the shape of the data-MC ratio across p_{T} and η_{det}, and at the same time provide stability against statistical fluctuations. Measurements in the region $|\eta_{\mathrm{det}}| > 2.7$ are excluded from the derivation of the correction function, and the residual correction for forward jets is fixed to the value obtained at $|\eta_{\mathrm{det}}| = 2.7$. All jets with a given p_{T} and $|\eta_{\mathrm{det}}| \geq 2.7$ therefore receive the same residual correction factor.

The resulting residual correction is shown as a black line in the lower panels of Figures 3 and 4. The line is solid over the range where the measurements are used to constrain the calibration, and dashed in the range where extrapolation is performed.

8.4. Systematic uncertainties

The observed difference in the relative response between data and simulation could be due to mis-modelling of physics or detector effects used in the simulation. All systematic uncertainties are derived as a function of p_{T} and $|\eta_{\mathrm{det}}|$, with no uncertainty assigned in the reference region ($|\eta_{\mathrm{det}}| < 0.8$). No statistically significant difference is observed for positive and negative η_{det} for any of the uncertainties.

---

[2] $F_{\mathrm{rel}}(p_{\mathrm{T}},\eta_{\mathrm{det}}) = \frac{\sum_{i=1}^{N_{\mathrm{bins}}} C_i w_i}{\sum_{i=1}^{N_{\mathrm{bins}}} w_i}$, $w_i = \frac{1}{\Delta C_i^2} \times \mathrm{Gaus}\left(\frac{\log p_{\mathrm{T}} - \log\left\langle p_{\mathrm{T}}^{\mathrm{probe}}\right\rangle_i}{\sigma_{p_{\mathrm{T}}}} \oplus \frac{\eta_{\mathrm{det}} - \langle\eta_{\mathrm{det}}\rangle_i}{\sigma_\eta}\right)$,
where i denotes the index of a $(p_{\mathrm{T}}^{\mathrm{avg}},\eta_{\mathrm{det}})$-bin, ΔC_i is the statistical uncertainty of C_i, $\left\langle p_{\mathrm{T}}^{\mathrm{probe}}\right\rangle_i$ and $\langle\eta_{\mathrm{det}}\rangle_i$ are the average p_{T} and η_{det} of the probe jets in the bin, Gaus(x) is the amplitude of a Gaussian function with $\mu = 0$ and $\sigma = 1$, $\sigma_{p_{\mathrm{T}}}$ and σ_η are width-parameters of the Gaussian kernel and $\oplus$ denotes addition in quadrature.The kernel width parameters varied with p_{T}, with stronger smoothing applied in low p_{T} ranges to reduce effects from statistical fluctuations: $\sigma_{p_{\mathrm{T}}} = 0.55$ and $\sigma_\eta = 0.16$ for $p_{\mathrm{T}} = 25$ GeV transitioning smoothly to $\sigma_{p_{\mathrm{T}}} = 0.28$ and $\sigma_\eta = 0.12$ for $p_{\mathrm{T}} = 50$ GeV and beyond.

The Sherpa and PowhegPythia8 are used to assess the physics modelling uncertainty. Both of these generators are accurate to leading-order in QCD for variables sensitive to the third jet modelling (such as the dijet balance). Since there is no *a priori* reason to trust one generator over the other, the difference between the two predictions is used to assess the modelling uncertainty. For $0.8 \leq |\eta_{\mathrm{det}}| < 2.7$, where data are corrected to the Sherpa predictions, the full difference between PowhegPythia8 and Sherpa is taken as the uncertainty. For $|\eta_{\mathrm{det}}| \geq 2.7$, where the calibration is frozen, the uncertainty is taken as the maximum difference between the calibration and either PowhegPythia8 or Sherpa MCs. The use of these event generators results in a substantial improvement in the agreement between the theoretical predictions, thus reducing the modelling-based uncertainty by a factor of approximately two with respect to the previous result [40]. Despite this improvement, this modelling uncertainty remains the largest systematic uncertainty in the measurement.

The physics modelling uncertainty on the relative response can also be cross-checked at particle-level by varying the PowhegPythia8 predictions. First, the renormalisation and factorisation scales in the Powheg Box are each varied by a factor of 0.5 and 2.0. The change in the relative response is observed to be much smaller than the difference between the PowhegPythia8 and Sherpa relative responses. Secondly, the change in the particle-level relative response of the Powheg-Herwig sample with respect to the Powheg-Pythia8 sample is found to be similar to the difference in the particle-level relative response between the PowhegPythia8 and Sherpa samples. It is concluded that the difference between Sherpa and PowhegPythia8 is a good reflection of the underlying physics modelling uncertainty.

The event topology selection requires that the two leading jets have a $\Delta\phi$ separation greater than 2.5 radians. In order to assess the influence of this selection on the transverse momentum balance, the residual calibration is rederived after shifting the cut up and down by ± 0.3 radian. The maximum difference between the shifted and nominal calibrations is taken as the uncertainty.

To assess the impact of pile-up on the calibration the difference between low and high pile-up subsets is investigated. The data is divided into high and low μ subsets ($\mu < 14$ and $\mu \geq 17$), and high and low N_{PV} subsets ($N_{\mathrm{PV}} < 9$ and $N_{\mathrm{PV}} \geq 11$), where N_{PV} is the number of reconstructed primary vertices in the inner detector. The calibration is re-evaluated for each subset and the uncertainty due to pile-up effects is taken to be the maximum fractional difference between the varied and nominal calibrations.

To assess the uncertainty on the calibration due to the JVF requirement on jets, the JVF cut is shifted up and down following the recommendations for the chosen operating point [34]. The up/down variations account for the extent to which JVF is mis-modelled for jets originating from the primary interaction vertex. The calibration is re-evaluated for both the JVF-up and JVF-down cases and the uncertainty is taken as the maximum fractional difference between the JVF-varied calibration and the nominal calibration.

The jet energy resolution (JER) [41] in the simulation is comparable to the resolution observed in data. To assess the impact of the JER on the transverse momentum balance, the jet energies in simulated events are smeared using a Gaussian function with width set to the JER uncertainty in the data. The difference between the calibrations obtained with nominal and smeared simulation is taken as the uncertainty due to JER effects.

The total systematic uncertainty is obtained as the quadratic sum of the various components mentioned. Figure 5 presents a summary of the uncertainties as a function of η_{det} for two representative values of jet transverse momentum, namely $p_{\mathrm{T}} = 35$ GeV and $p_{\mathrm{T}} = 300$ GeV. The uncertainties have a strong pseudorapidity dependance, increasing with η_{det}, and have a weaker p_{T}-dependance, decreasing with increasing jet transverse momentum.

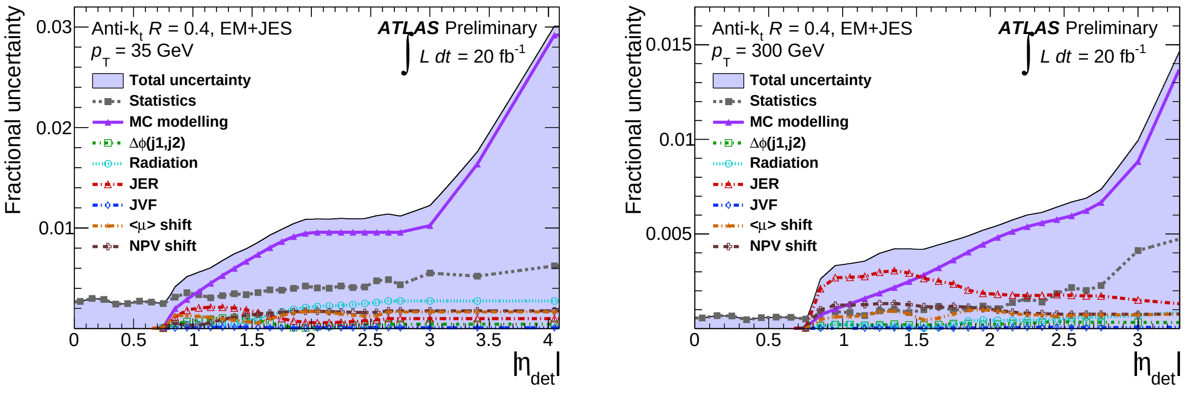

(a) (b)

Figure 5: Summary of uncertainties on the intercalibration as a function of the jet η_{det} for anti-k_t jets with $R = 0.4$ calibrated with the EM+JES scheme, separately for $p_{\mathrm{T}} = 35$ GeV (a) and $p_{\mathrm{T}} = 300$ GeV (b). The individual components are added in quadrature to obtain the total uncertainty. The modelling uncertainty is the dominant component.

9. Jet energy scale calibration for high-p_{T} jets using multijet events

9.1. Results

Figure 6(a) shows the MJB for data and MC simulation using the EM+JES calibration scheme. The data and MC simulation agree to within 1 % across the transverse momentum range probed, a feature that is reproduced by the Z/γ-jet analyses [36]. Only statistical uncertainties are shown, which are below 1 % up to 1.7 TeV.

9.2. Systematic Uncertainties

As the jets entering the MJB have been calibrated using the other *in situ* approaches, the uncertainty in the energy scale of the jets in the recoil system is defined by the systematic and statistical uncertainties on each *in situ* procedure. To propagate the uncertainty to the MJB, all input components are individually varied by $\pm 1\sigma$ and the full iterative analysis procedure repeated. Deviations in the MJB due to the statistical uncertainties of the γ+jet and Z+jet calibrations are typically much less than 1 %.

Secondly, the event selection criteria and the modelling in the event generators directly affect the p_{T} balance used to obtain the MJB results. The impact of the event selection criteria is investigated by shifting each cut up and down by a specified amount and observing the change in the MJB. The transverse momentum threshold for jets is shifted by ±5 GeV, the $p_{\mathrm{T}}^{\mathrm{asymm}} = p_{\mathrm{T}}^{\mathrm{jet}_2}/p_{\mathrm{T}}^{\mathrm{recoil}}$ is shifted by ± 0.1, the angle α is shifted by ± 0.1 and the angle β is shifted by ± 0.5. The uncertainty due to MC modelling of multijet events is estimated from the symmetrised envelope of MJB corrections obtained by comparing the nominal results obtained with Sherpa to those obtained with PowhegPythia8, Pythia8 and Herwig++.

The unknown parton flavour of each jet is also a cause of systematic uncertainty. The uncertainty on the MJB observable due to the jet flavour response is evaluated using a correlated propagation of the

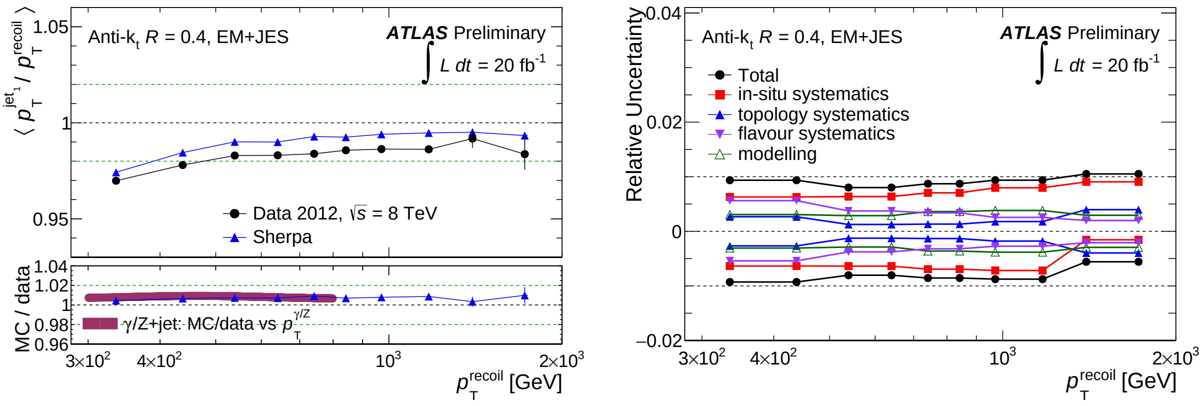

(a)

(b)

Figure 6: (a) Multijet balance in data and MC simulation for anti-k_t 0.4 jets calibrated with the EM+JES scheme. The magenta solid line compares the results to the γ/Z+jet results. (b) The impact of *in situ*, event selection (topology), physics modelling and jet flavour systematic uncertainties on the MJB.

jet flavour response uncertainties, i.e. all jets are shifted simultaneously. The jet flavour composition uncertainty is propagated to the MJB observable for the first, second and third recoil jets independently, with the final composition uncertainty obtained from the quadrature sum of the three variations. The total uncertainty due to the unknown parton flavour is taken as the sum in quadrature of the flavour response and composition uncertainties.

Examples of the impact of systematic uncertainties are shown in Figure 6(b), for anti-k_t 0.4 jets using the EM+JES calibration scheme. The uncertainties are grouped together into *in-situ*, event topology, physics modelling and jet flavour categories. Uncertainties for anti-k_t 0.6 jets or the LCW+JES scheme are comparable.

10. Jet energy resolution determination using dijet events

Figure 7 shows the measured jet energy resolution at a function of p_T^{avg} for EM+JES jets, for jets that fall into different regions of the calorimeter. The results are presented for both the dijet balance and bisector methods and good agreement is seen between the methods for all values of p_T^{avg} and $|\eta_{det}|$. The jet energy resolution in simulated events is also shown as a dotted line and is in agreement with the measured JER in data. The JER in simulation is determined by geometrical matching of particle-level jets to calorimeter jets and is defined, for a given value of particle-jet transverse momentum, by the width of the response distribution $(p_T^{reco} - p_T^{part})/p_T^{reco}$.

10.1. Systematic Uncertainties

The JER is determined in data by subtracting a particle-level asymmetry from the measured asymmetry as discussed in Section 6. The particle-level asymmetry is defined as the weighted average of the particle-level asymmetries obtained for each of the Sherpa, PowhegPythia8, Pythia8 and Herwig++ event samples. The uncertainty on this weighted average is taken to be the RMS of the particle-level

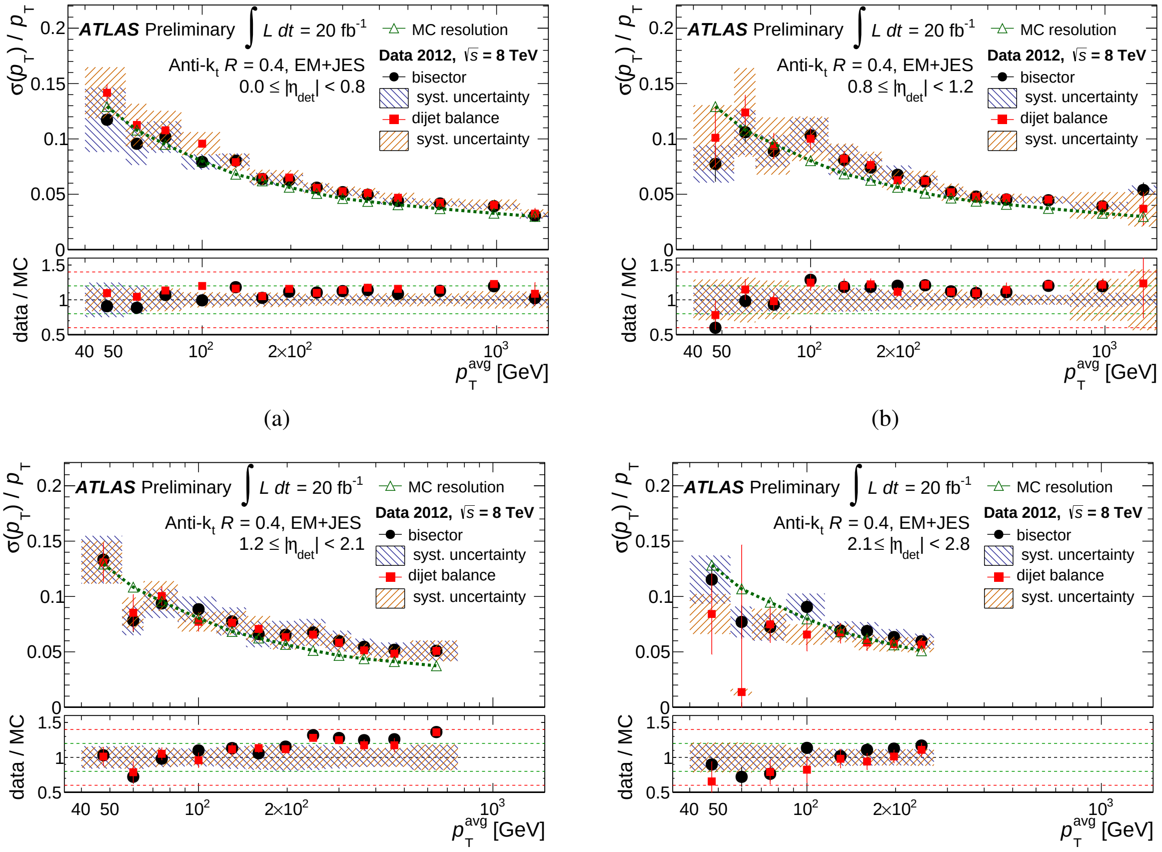

(a) (b)

(c) (d)

Figure 7: Jet energy resolution obtained for EM+JES calibrated jets as a function of the jet transverse momentum in four regions of detector pseudorapidity: (a) $|\eta_{\mathrm{det}}| < 0.8$ (b) $0.8 \leq |\eta_{\mathrm{det}}| < 1.2$, (c) $1.2 \leq |\eta_{\mathrm{det}}| < 2.1$ and (d) $2.1 \leq |\eta_{\mathrm{det}}| < 2.8$. The green and red dashed lines indicate $1 \pm 20\,\%$ and $1 \pm 40\,\%$ respectively.

asymmetries obtained from the four event generators. This source of uncertainty is typically 2 % at low-$p_{\mathrm{T}}^{\mathrm{avg}}$ for both methods, falling to less than 1 % at the highest-$p_{\mathrm{T}}^{\mathrm{avg}}$.

The non-closure of the particle-level subtraction is investigated using simulation and treated as a systematic uncertainty in the method. The weighted average of the particle level asymmetries predicted by Sherpa, PowhegPythia8, Pythia and Herwig++ is subtracted in quadrature from the weighted average of the associated calorimeter asymmetries. The non-closure is typically about (10 − 15) % for the bisector method, but it is larger for the dijet balance method, reaching 25 % in some regions.

Finally, there are a number of systematic uncertainties that arise from experimental sources. The uncertainty in the JES calibration is investigated by shifting the energy of the jets by the $\pm 1\sigma$ uncertainty, with a typical effect between 5 % and 10 % at low-$p_{\mathrm{T}}^{\mathrm{avg}}$. The uncertainty due to the choice of JVF cut is observed to have a less than 2 % effect for both methods. The uncertainty due to the cut on the azimuthal angle between the jets is investigated by changing the cut values by ±0.3, with a negligible effect at high-$p_{\mathrm{T}}^{\mathrm{avg}}$ for both methods, a small (< 4 %) effect on the dijet balance results at low-$p_{\mathrm{T}}^{\mathrm{avg}}$ and a larger effect (5 − 15) % on the bisector results at low-$p_{\mathrm{T}}^{\mathrm{avg}}$. The impact of the veto on the third jet is investigated by changing the cut value by ±4 GeV, and is found to have a (10 − 15) % effect at low-$p_{\mathrm{T}}^{\mathrm{avg}}$ for both methods, falling to a few percent at the higher $p_{\mathrm{T}}^{\mathrm{avg}}$ values.

The total systematic uncertainty is taken to be the sum in quadrature of all other sources of uncertainty.

11. Summary and conclusions

The response of the ATLAS calorimeter to jets has been studied using proton-proton collisions at $\sqrt{s}$ = 8 TeV recorded by the ATLAS experiment in 2012. Jet energy scale calibrations and uncertainties have been derived as a function of transverse momentum and pseudorapidity. The jet energy resolution has also been measured as a function of jet transverse momentum and pseudorapidity.

The pseudorapidity dependence of the jet response is studied relative to a central reference region by evaluating the transverse momentum balance in dijet events. A residual transverse momentum and pseudorapidity-dependent jet calibration is derived for jets in data, in order to correct for effects not captured by the default calibration derived using MC simulation. These calibration factors range from 0.96 to 1.02 depending on the pseudorapidity of the jet. The uncertainties on these calibration factors have been significantly reduced compared to previous results using event generators with improved modelling of multijet production; they are typically below 1 % for central jets rising to 3.5 % for low transverse momentum jets at high absolute pseudorapidity.

The jet energy scale calibration for central jets with high transverse momentum has been determined using events in which an isolated high transverse momentum jet recoils against a system of low transverse momentum jets. The data and simulation are found to agree to better than 1 % for jets with transverse momentum up to 1.7 TeV, with an associated uncertainty of less than 1 %.

The jet energy resolution has been measured as a function of jet transverse momentum and pseudorapidity using the transverse momentum balance of jets in dijet events. Two methods are used with differing sensitivity to underlying physics effects. In general, it is found that the jet energy resolution in data is well reproduced in the simulation.

All results presented in the previous sections correspond to anti-k_t R=0.4 jets calibrated with the EM+JES scheme. Results for anti-k_t R=0.4 jets calibrated using the LCW+JES scheme are available in Appendix A.

A. Appendix: Results for anti-k_t $R = 0.4$ jets calibrated with the LCW+JES scheme

A.1. Relative jet energy scale calibration using dijet events

A.1.1. Comparison of matrix and central reference methods

Figure 8 compares the relative jet response calculated using the matrix method to that obtained with the central reference methods for anti-k_t jets with $R = 0.4$ calibrated with the LCW+JES scheme.

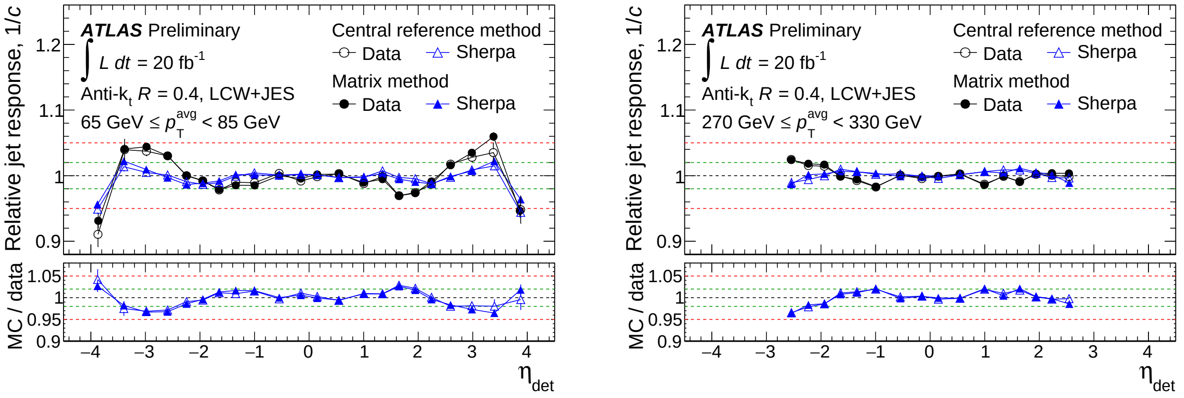

(a)

(b)

Figure 8: Relative response measured using the matrix and the central reference methods for anti-k_t jets with $R = 0.4$ calibrated with the LCW+JES scheme as a function of the probe jet pseudorapidity. Results are presented for 65 GeV $\leq p_{\mathrm{T}}^{\mathrm{avg}} <$ 85 GeV and 270 GeV $\leq p_{\mathrm{T}}^{\mathrm{avg}} <$ 330 GeV. The green and red dashed lines indicate 1 ± 2 % and 1 ± 5 % respectively.

A.1.2. Comparison of data with simulation

Figure 9 shows the relative response as a function of the jet pseudorapidity for anti-k_t jets with $R = 0.4$ calibrated with the LCW+JES scheme. Data and the MC simulations are presented for four different $p_{\mathrm{T}}^{\mathrm{avg}}$ regions: 25 GeV $\leq p_{\mathrm{T}}^{\mathrm{avg}} <$ 40 GeV, 85 GeV $\leq p_{\mathrm{T}}^{\mathrm{avg}} <$ 115 GeV, 220 GeV $\leq p_{\mathrm{T}}^{\mathrm{avg}} <$ 270 GeV and 760 GeV $\leq p_{\mathrm{T}}^{\mathrm{avg}} <$ 1200 GeV. Figure 10 shows the relative response as a function of $p_{\mathrm{T}}^{\mathrm{avg}}$ for anti-k_t jets with $R = 0.4$ calibrated with the LCW+JES scheme. Results presented for two representative η_{det}-bins, namely $-1.5 \leq \eta_{\mathrm{det}} < -1.2$ and $2.1 \leq \eta_{\mathrm{det}} < 2.4$.

Small differences are observed in the response at low $p_{\mathrm{T}}^{\mathrm{avg}}$ when comparing the LCW+JES and EM+JES calibrations between Figure 9 and Figure 3. Intrinsic differences between the LCW+JES and EM+JES calibration schemes can lead to different low $p_{\mathrm{T}}^{\mathrm{avg}}$ behaviour. However, this difference is well modelled in the simulation, which is important because it is the relative difference between data and MC that is used for deriving the calibration.

A.1.3. Systematic uncertainties

Figure 11 presents a summary of the uncertainties as a function of η_{det} for anti-k_t jets with $R = 0.4$ calibrated with the LCW+JES scheme. Results presented for two representative values of jet transverse momentum, namely $p_{\mathrm{T}} = 35$ GeV and $p_{\mathrm{T}} = 300$ GeV.

Comparing Figures 5(b) and 11(b), it is apparent that the uncertainty on the calibration due to the JER uncertainty is not the same for the two calibration schemes. The different behaviour is found to be due to the procedure for deriving and applying the resolution smearing factors, whereby jets calibrated with the EM+JES or LCW+JES schemes receive quite different smearing factors depending on the jet p_{T} and η_{det}. Excluding the JER uncertainty, all components are generally consistent in shape and similar in magnitude across $p_{\mathrm{T}}^{\mathrm{avg}}$ and η_{det}, with LCW+JES uncertainties being slightly larger at low $p_{\mathrm{T}}^{\mathrm{avg}}$.

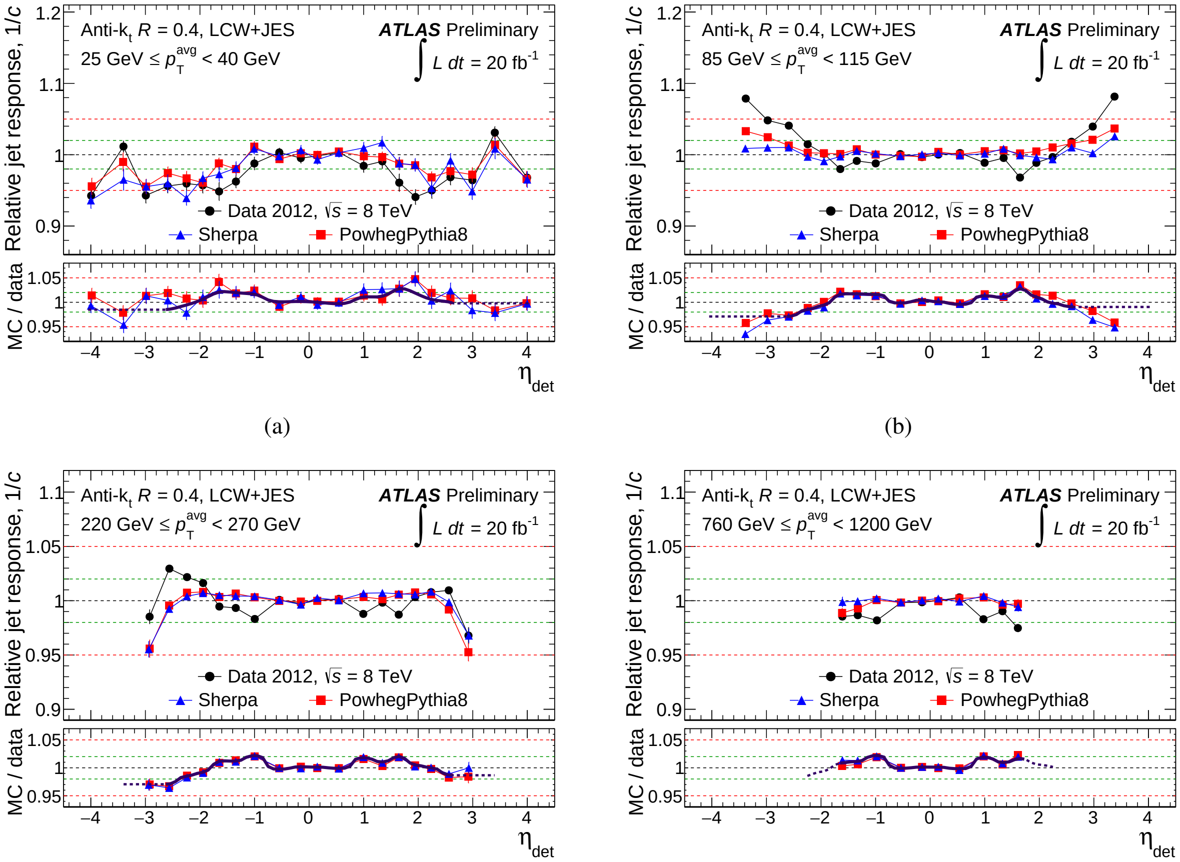

(a) (b) (c) (d)

Figure 9: Relative jet response, $1/c$, as a function of the jet pseudorapidity for anti-k_t jets with $R = 0.4$ calibrated with the LCW+JES scheme, separately for 25 GeV $< p_T^{avg} <$ 40 GeV, 85 GeV $< p_T^{avg} <$ 115 GeV, 220 GeV $< p_T^{avg} <$ 270 GeV and 760 GeV $< p_T^{avg} <$ 1200 GeV. The lower parts of the figures show the ratios between the data and MC relative response. These measurements are performed using the matrix method. The green and red dashed lines indicate 1 ± 2 % and 1 ± 5 % respectively.

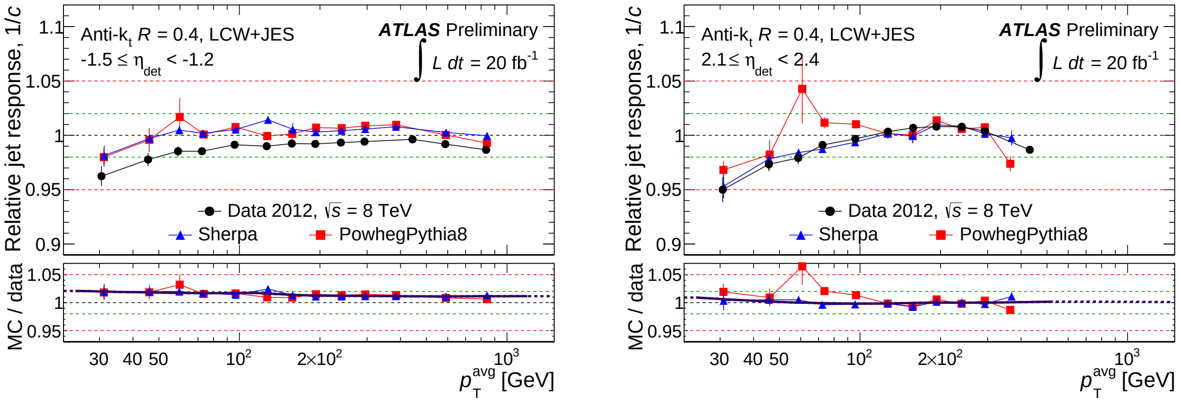

(a)

(b)

Figure 10: Relative jet response, $1/c$, as a function of the jet p_T for anti-k_t jets with $R = 0.4$ calibrated with the LCW+JES scheme, separately for $-1.5 \leq \eta_{\mathrm{det}} < -1.2$ and $2.1 \leq \eta_{\mathrm{det}} < 2.4$. The lower parts of the figures show the ratios between the data and MC relative response. The green and red dashed lines indicate $1 \pm 2\,\%$ and $1 \pm 5\,\%$ respectively.

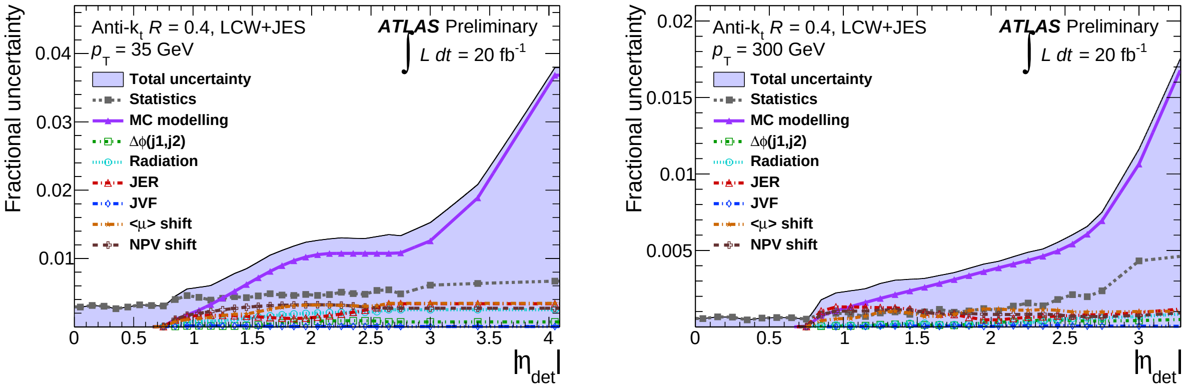

(a)

(b)

Figure 11: Summary of uncertainties on the intercalibration as a function of the jet η_{det} for anti-k_t jets with $R = 0.4$ calibrated with the LCW+JES scheme, separately for $p_T = 35$ GeV (a) and $p_T = 300$ GeV (b). The individual components are added in quadrature to obtain the total uncertainty. The modelling uncertainty is the dominant component.

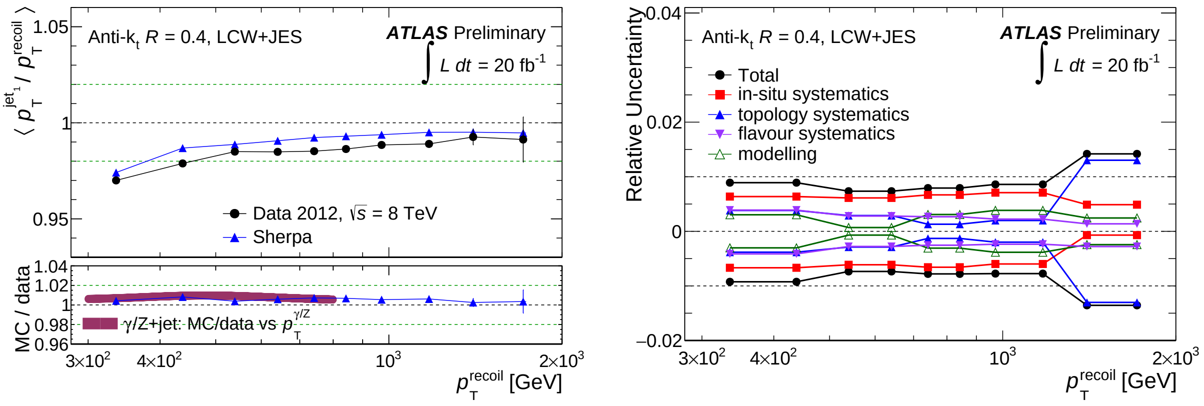

(a)

(b)

Figure 12: (a) Multijet balance in data and MC simulation for anti-k_t 0.4 jets calibrated with the LCW+JES scheme. The magenta solid line compares the results to the γ/Z+jet results. (b) The impact of *in situ*, event selection (topology), physics modelling and jet flavour systematic uncertainties on the MJB.

A.2. Jet energy scale calibration for high-p_T jets using multijet events

Figure 12(a) shows the MJB for data and MC simulation using anti-k_t $R = 0.4$ jets using the LCW+JES calibration scheme. The data and MC simulation agree to within 1 % across the transverse momentum range probed, a feature that is reproduced by the Z/γ-jet analyses. Only statistical uncertainties are shown, which are below 1 % up to 1.7 TeV. Systematic uncertainties are shown in Figure 12(b). The increase in the topology uncertainty at high p_T^{recoil} is the result of a statistical fluctuation due to low statistics in that region after the tightest values of the α and β cuts.

A.3. Jet energy resolution determination using dijet events

Figure 13 shows the measured jet energy resolution at a function of p_T^{avg} for LCW+JES jets, for jets that fall into different regions of the calorimeter. The results are presented for both the dijet balance and bisector methods and good agreement is seen between the methods for all values of p_T^{avg} and $|\eta_{det}|$.

References

[1] ATLAS Collaboration, *Jet energy measurement with the ATLAS detector in proton-proton collisions at $\sqrt{s} = 7$ TeV*, Eur. Phys. J. **C 73** (2013) 2304, `arXiv:1112.6426 [hep-ex]`.

[2] ATLAS Collaboration, *The ATLAS experiment at the CERN Large Hadron Collider*, JINST **3** (2008) S08003.

[3] ATLAS Collaboration, *Performance of the ATLAS Trigger System in 2010*, Eur. Phys. J. **C 72** (2012) 1849, `arXiv:1110.1530 [hep-ex]`.

[4] P. Nason, *A New method for combining NLO QCD with shower Monte Carlo algorithms*, JHEP **11** (2004) 040, `arXiv:hep-ph/0409146 [hep-ph]`.

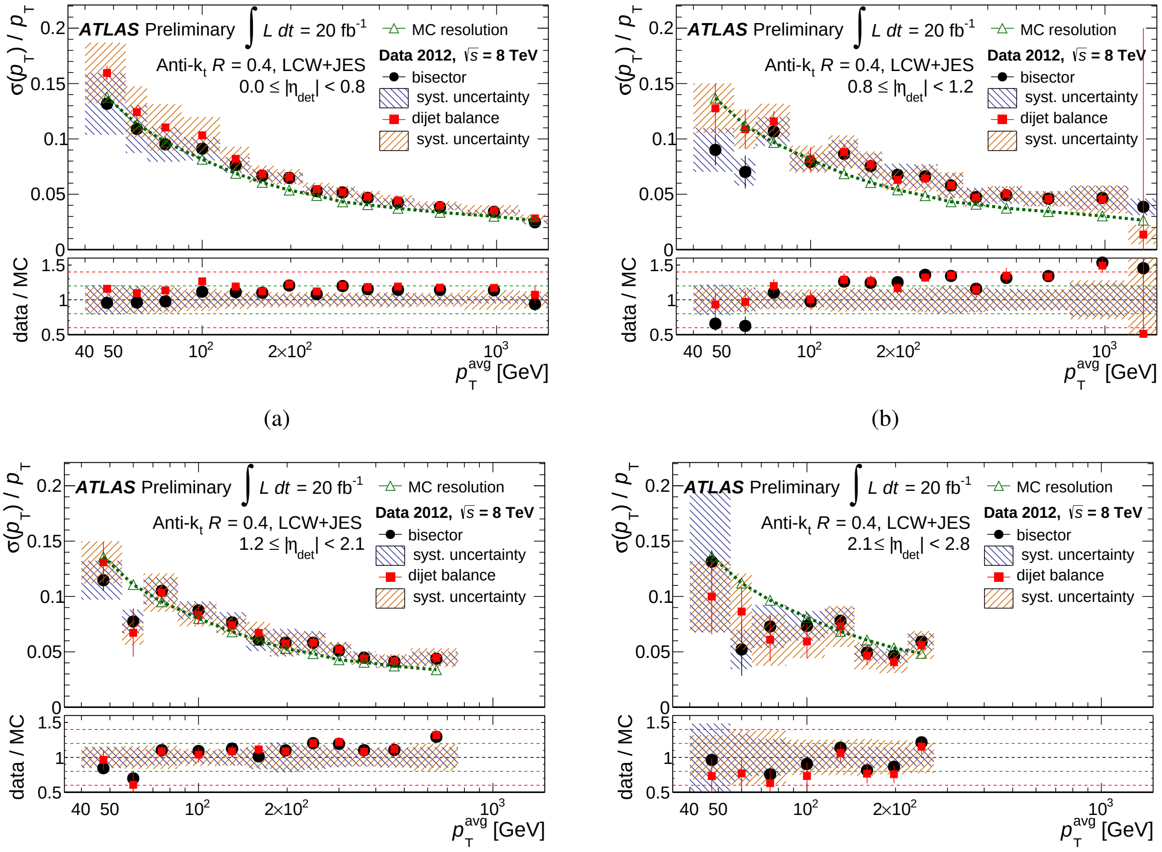

(a)

(b)

(c)

(d)

Figure 13: Jet energy resolution obtained for LCW+JES calibrated jets as a function of the jet transverse momentum in four regions of detector pseudorapidity: (a) $|\eta_{\mathrm{det}}| < 0.8$ (b) $0.8 \leq |\eta_{\mathrm{det}}| < 1.2$, (c) $1.2 \leq |\eta_{\mathrm{det}}| < 2.1$ and (d) $2.1 \leq |\eta_{\mathrm{det}}| < 2.8$. The green and red dashed lines indicate 1 ± 20 % and 1 ± 40 % respectively.

[5] S. Frixione, P. Nason, and C. Oleari, *Matching NLO QCD computations with Parton Shower simulations: the POWHEG method*, JHEP **11** (2007) 070, `arXiv:0709.2092 [hep-ph]`.

[6] S. Alioli et al., *A general framework for implementing NLO calculations in shower Monte Carlo programs: the POWHEG BOX*, JHEP **06** (2010) 043, `arXiv:1002.2581 [hep-ph]`.

[7] T. Gleisberg et al., *Event generation with SHERPA 1.1*, JHEP **02** (2009) 007, `arXiv:0811.4622 [hep-ph]`.

[8] T. Sjostrand, S. Mrenna, and P. Z. Skands, *A Brief Introduction to PYTHIA 8.1*, Comput. Phys. Commun. **178** (2008) 852–867, `arXiv:0710.3820 [hep-ph]`.

[9] S. Gieseke et al., *Herwig++ 1.0: An Event generator for e+ e- annihilation*, JHEP **02** (2004) 005, `arXiv:hep-ph/0311208 [hep-ph]`.

[10] J. Bellm et al., *Herwig++ 2.7 Release Note*, `arXiv:1310.6877 [hep-ph]`.

[11] S. Alioli et al., *Jet pair production in POWHEG*, JHEP **1104** (2011) 081, `arXiv:1012.3380 [hep-ph]`.

[12] H.-L. Lai et al., *New parton distributions for collider physics*, Phys. Rev. **D 82** (2010) 074024, `arXiv:1007.2241 [hep-ph]`.

[13] ATLAS Collaboration, *New ATLAS event generator tunes to 2010 data*, ATL-PHYS-PUB-2011-008, CERN, Geneva, Apr, 2011.

[14] ATLAS Collaboration, *Further ATLAS tunes of PYTHIA6 and Pythia 8*, ATL-PHYS-PUB-2011-014, CERN, Geneva, Nov, 2011.

[15] S. Catani et al., *QCD matrix elements + parton showers*, JHEP **11** (2001) 063, `arXiv:hep-ph/0109231 [hep-ph]`.

[16] *Summary of ATLAS Pythia 8 tunes*, ATL-PHYS-PUB-2012-003, CERN, Geneva, Aug, 2012.

[17] S. Gieseke, C. Rohr, and A. Siodmok, *Colour reconnections in Herwig++*, Eur. Phys. J. **C 72** (2012) 2225. `http://dx.doi.org/10.1140/epjc/s10052-012-2225-5`.

[18] GEANT4 Collaboration, S. Agostinelli et al., *GEANT4: A simulation toolkit*, Nucl. Instrum. Meth. **A 506** (2003) 250–303.

[19] ATLAS Collaboration, *The ATLAS simulation infrastructure*, Eur. Phys. J. **C 70** (2010) 823–874, `arXiv:1005.4568 [physics.ins-det]`.

[20] G. Folger and J. Wellisch, *String parton models in GEANT4*, `arXiv:nucl-th/0306007`.

[21] A. Ribon et al., *Status of Geant4 hadronic physics for the simulation of LHC experiments at the start of the LHC physics program*, CERN-LCGAPP-2010-02 [http://lcgapp.cern.ch/project/docs/noteStatusHadronic2010.pdf].

[22] ATLAS Collaboration, *Summary of ATLAS Pythia 8 tunes*, ATL-PHYS-PUB-2012-003, CERN, Geneva, Aug, 2012.

[23] A. Martin et al., *Parton distributions for the LHC*, Eur. Phys. J. **C 63** (2009) 189–285, `arXiv:0901.0002 [hep-ph]`.

[24] M. Cacciari, G. P. Salam, and G. Soyez, *The anti-k_t jet clustering algorithm*, JHEP **04** (2008) 063, `arXiv:0802.1189 [hep-ph]`.

[25] M. Cacciari and G. P. Salam, *Dispelling the N^3 myth for the k_t jet-finder*, Phys. Lett. **B 641** (2006) 57–61.

[26] M. Cacciari, G. P. Salam, and G. Soyez. http://fastjet.fr/.

[27] W. Lampl et al., *Calorimeter clustering algorithms: description and performance*, ATL-LARG-PUB-2008-002 [http://cdsweb.cern.ch/record/1099735], April, 2008.

[28] C. Cojocaru et al., *Hadronic calibration of the ATLAS liquid argon end-cap calorimeter in the pseudorapidity region* $1.6 < |\eta| < 1.8$ *in beam tests*, Nucl. Instrum. Meth. **A 531** (2004) 481–514.

[29] M. Aharrouche et al., *Measurement of the response of the ATLAS liquid argon barrel calorimeter to electrons at the 2004 combined test-beam*, Nucl. Instrum. Meth. **A 614** (2010) 400–432.

[30] J. Colas et al., *Response uniformity of the ATLAS liquid argon electromagnetic calorimeter*, Nucl. Instrum. Meth. **A 582** (2007) 429–455, `arXiv:0709.1094 [physics.ins-det]`.

[31] M. Aharrouche et al., *Energy linearity and resolution of the ATLAS electromagnetic barrel calorimeter in an electron test-beam*, Nucl. Instrum. Meth. **A 568** (2006) 601–623.

[32] ATLAS Collaboration, *Electron performance measurements with the ATLAS detector using the 2010 LHC proton-proton collision data*, Eur. Phys. J. **C 72** (2012) 1909, `arXiv:1110.3174 [hep-ex]`.

[33] T. Barillari et al., *Local Hadronic Calibration*, ATL-LARG-PUB-2009-001-2, CERN, Geneva, Jun, 2008.

[34] ATLAS Collaboration, *Pile-up subtraction and suppression for jets in ATLAS*, ATLAS-CONF-2013-083, CERN, Geneva, Aug, 2013.

[35] ATLAS Collaboration, *Jet global sequential corrections with the ATLAS detector in proton-proton collisions at sqrt(s) = 8 TeV*, ATLAS-CONF-2015-002, CERN, Geneva, Mar, 2015.

[36] ATLAS Collaboration, *Determination of the jet energy scale and resolution at ATLAS using Z/γ-jet events in data at $\sqrt{s} = 8$ TeV*, In preparation.

[37] ATLAS Collaboration, *Data-Quality Requirements and Event Cleaning for Jets and Missing Transverse Energy Reconstruction with the ATLAS Detector in Proton-Proton Collisions at a Center-of-Mass Energy of $sqrts = 7$ TeV*, ATLAS-CONF-2010-038, CERN, Geneva, Jul, 2010.

[38] M. Cacciari and G. P. Salam, *Pileup subtraction using jet areas*, Phys. Lett. **B 659** (2008) 119–126, `arXiv:0707.1378 [hep-ph]`.

[39] V. Lendermann et al., *Combining Triggers in HEP Data Analysis*, Nucl. Instrum. Meth. **A 604** (2009) 707–718, `arXiv:0901.4118 [hep-ex]`.

[40] ATLAS Collaboration, *Jet energy measurement and its systematic uncertainty in proton-proton collisions at $\sqrt{s} = 7$ TeV with the ATLAS detector*, Eur. Phys. J. **C 75** (2015) 17, `arXiv:1406.0076 [hep-ex]`.

[41] ATLAS Collaboration, *Jet energy resolution in proton-proton collisions at $\sqrt{s} = 7$ TeV recorded in 2010 with the ATLAS detector*, Eur. Phys. J. **C 73** (2013) 2306, `arXiv:1210.6210 [hep-ex]`.